instruments

MDPI

Article

Design and Simulation of a Muon Detector Using Wavelength-Shifting Fiber Readouts for Border Security

Anzori Sh. Georgadze [1,2]

[1] Institute of Physics, Tartu University, W. Ostwaldi 1, 50411 Tartu, Estonia; anzori.heorhadze@ut.ee or georgadze@kinr.kiev.ua
[2] Institute for Nuclear Research, National Academy of Sciences of Ukraine, Prospekt Nauky 47, 03680 Kyiv, Ukraine

Abstract: Cosmic ray muon tomography is a promising method for the non-invasive inspection of shipping containers and trucks. It leverages the highly penetrating cosmic muons and their interactions with various materials to generate three-dimensional images of large and dense objects, such as inter-modal shipping containers, which are typically opaque to conventional X-ray radiography techniques. One of the key tasks of customs and border security is verifying shipping container declarations to prevent illegal trafficking, and muon tomography offers a viable solution for this purpose. Common imaging methods using muons rely on data analysis of either muon scattering or absorption–transmission. We design a compact muon tomography system with dimensions of $3 \times 3 \times 3$ m^3, consisting of 2D position-sensitive detectors. These detectors include plastic scintillators, wavelength-shifting (WLS) fibers, and SiPMs. Through light transport modeling with GEANT4, we demonstrate that the proposed detector design—featuring 1 m $\times$ 1 m scintillator plates with 2 mm^2 square-shaped WLS fibers—can achieve a spatial resolution of approximately 0.7–1.0 mm. Through Monte Carlo simulations, we demonstrate that combining muon scattering and absorption data enables the rapid and accurate identification of cargo materials. In a smuggling scenario where tobacco is falsely declared as paper towel rolls, this combined analysis distinguishes the two with 3 σ confidence at a spatial resolution of 1 mm (FWHM) for the muon detector, achieving results within a scanning time of 40 s for a 20-foot shipping container.

Keywords: muon tomography; GEANT4; tracking detectors; detection of contraband

Academic Editor: Antonio Ereditato

Received: 26 December 2024
Revised: 21 January 2025
Accepted: 23 January 2025
Published: 27 January 2025

Citation: Georgadze, A.S. Design and Simulation of a Muon Detector Using Wavelength-Shifting Fiber Readouts for Border Security. *Instruments* **2025**, *9*, 1. https://doi.org/10.3390/instruments9010001

1. Introduction

Muon tomography is an innovative and versatile imaging technique with the potential to revolutionize fields ranging from security to scientific research [1–6]. Its unique properties, such as non-invasiveness, deep penetration, and material sensitivity, make it a valuable asset for solving complex challenges in border security. Muon tomography utilizes naturally occurring cosmic-ray muons to non-invasively probe the internal structures of large objects, like shipping containers or trucks. Its unique capabilities, such as a high penetration power and sensitivity to material density and composition, make it a promising tool in border security applications.

High-energy muons are constantly generated in the Earth's atmosphere from cosmic rays. These particles have significant penetration capabilities, allowing them to pass through dense materials that conventional imaging techniques cannot. As muons pass through matter, they interact with atoms through processes such as bremsstrahlung, pair production, photo-nuclear interactions, and multiple Coulomb scattering. Muon tomography uses a scattering angle that is proportional to the atomic number (Z) of the material. By placing detectors around a target object, the trajectories of muons entering and exiting the object are tracked. The scattering and

absorption patterns of the muons are analyzed to reconstruct a 3D density map of the object's interior, identifying different materials or illegal objects hidden inside cargo.

Due to its penetrating properties, muon tomography has been proposed as a tool for border security applications to scan cargo containers and vehicles for hidden contraband or illicit materials [7–17]. The European project "Cosmic Beam Tomograph for Identification of Hazardous and Illegal Goods Hidden in Trucks and Sea Containers" (SilentBorder) [18] focuses on the development and in situ testing of a high-tech scanner designed for border guards, customs, and law enforcement authorities to inspect shipping containers at border control points. To improve the accuracy of inspection of the contents of shipping containers and trucks, an approach has been developed combining muon scattering and absorption [19–22]. Using a tobacco smuggling example in which cigarettes are disguised as rolls of paper towels, it was demonstrated that a muon tomography system (MTS) that completely covers a 20-foot shipping container (8 m $\times$ 4 m $\times$ 3 m in size) can distinguish cigarettes from rolls of paper towels in about 10 s.

The purpose of this study is to develop a muon tracking detector with high detection efficiency and high positional resolution for border security applications. We proposed a position-sensitive detector comprising a large-area plastic scintillator readout using wavelength-shifting (WLS) fibers. The detector's positional resolution was evaluated through simulations of light transport using the GEANT4 toolkit. Furthermore, we assessed the material discrimination capability of a small-scale MTS ($3 \times 3 \times 3$ m^3) incorporating novel scintillator-WLS fiber-based muon detectors. The compact MTS developed is considered a cost-effective solution for a cargo scanning portal. This system enables shipping containers to move continuously through the MTS while maintaining high throughput in container verification.

2. Simulation of the Muon Detector

The muon detector is composed of a plastic scintillator slab of size $100 \times 100 \times 1$ cm^3. Two arrays of 485 square-shaped WLS fibers ($2 \times 2 \times 1000$ mm^3) are attached to either side of the plastic scintillator slab (see Figure 1a). The WLS fiber arrays are orthogonal to each other and represent the light distribution in the x and y directions. The light photons produced by muon particles inside the plastic scintillator are absorbed by the WLS fibers, and the re-emitted green light are guided by total internal reflection to the two silicon photomultipliers (SiPMs) that are connected to both ends of each WLS fiber. The WLSFs are optically coupled to a scintillator using an optical adhesive. The fibers are approximately 0.062 mm apart from each other. The outer detector layer, which covers the WLS fibers on the top and bottom, is made of an enhanced specular reflector (ESR) film to reflect photons back into the fibers. WLS fibers provide readouts at both ends using SiPMs. To prevent reflections from the lateral faces of the crystals, they are painted black.

The simulation of optical photons is based on the Monte Carlo code GEANT4 [23]. The transport of light photons simulated using GEANT4 is shown in Figure 1b. In the GEANT4 simulation of the plastic scintillator–WLS detector, all relevant physical processes are included to ensure accurate modeling of photon interactions within the detector. The following electromagnetic processes, such as ionization, bremsstrahlung, multiple Compton scattering, pair production, Compton scattering, and the photoelectric effect, are considered. Optical processes include scintillation, Cherenkov radiation, volume absorption, Rayleigh scattering, and boundary processes like reflection, refraction, and absorption. The Birk's effect, which adjusts the scintillation light yield to account for variations in the energy deposition density by ionizing particles, is accounted for. For optical photon transport, the GLISUR model [24,25] in the GEANT4 package was used. This model simulates the interactions of optical photons at the interfaces between different materials by applying the concept of optical surfaces to describe light reflection and transmission at the boundaries

between media, accounting for scattering, absorption, and reflection. In the detector GEANT4 model, we define the surface roughness for all interfaces. When the polish parameter is set to zero, it represents maximum roughness, where photons are reflected according to a Lambertian distribution. Conversely, a polish value of one applies Snell's Law. For each surface, the appropriate optical boundary processes and reflectivity are specified. In the simulation, the refractive index of the plastic scintillator is set to 1.58, the light yield is set to 10,000 photons/MeV, and the light attenuation length is set to 240 cm [26]. The WLS fiber used in simulations is the square shape double clad BCF-91A [27], which has an absorption peak at 420 nm and an emission peak at 494 nm. The plastic scintillator light emission peak is at 420–430 nm and is a good match to the BCF-91A maximum absorption wavelength range (410–460 nm). As show in Figure 2 the absorption spectrum of the fiber matches the emission spectrum of the BC-408 scintillator, providing maximal light conversion for transmission to WLS fibers. The WLS fibers are bonded to the SiPMs using silicone optical grease to enhance the light transmission efficiency of the SiPM, whose entrance window is made of epoxy resin with a refractive index of 1.5. The polystyrene core refractive index of BCF-91A WLS fibers is 1.6, while that of the first cladding layer (acrylic) has a refractive index of 1.49 and the second cladding layer (fluor-acrylic) has a refractive index of 1.42. To attach the fibers to the scintillator plate, an optical adhesive with a refractive index of n = 1.32 is used. The SiPMs are modeled as a Si material and the SiPM window size is 2 × 2 mm^2 and is made of epoxy resin with a refractive index of n = 1.52. To improve light detection, SiPMs are coupled with WLSFs with an optical coupling material with a refractive index of 1.465. The light detection efficiency is determined by weighting the SiPM PDE with the BCF-91A WLS fiber emission spectra, which gives a value of ≈40%. The developed simulation model and optical properties of the materials are verified based on experimental data on the light response of a plastic scintillator and WLS fibers, as described in [28].

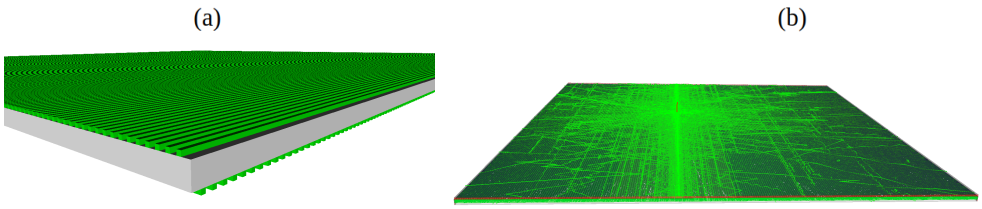

Figure 1. (**a**) GEANT4 visualization of a detector composed of a plastic scintillator readout provided by 2 × 2 mm^2 WLS fibers. (**b**) Simulated light photons transmitted through a plastic scintillator slab and WLS fibres with GEANT4. Generated scintillation photons, shown as light green lines. The SiPMs are depicted in red.

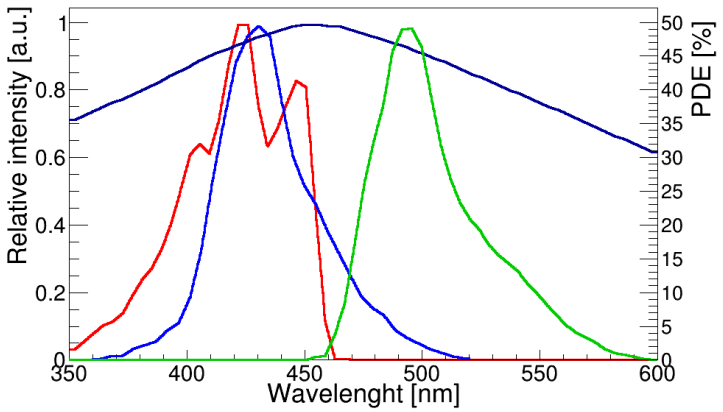

Figure 2. Photon emission spectrum of BC-404 scintillator [29] (blue colour); absorption (red colour) and emission (green colour) spectra of BCF-91A [27] and SiPM PDE (dark blue colour).

3. Simulation Results

We simulate a muon of 3 GeV energy passing through the plastic scintillator detector. The energy deposited in the scintillator is converted into fluorescence and finally to light photons. The generated optical photons pass directly through the plastic scintillator plate to the black-painted side surfaces of the detector and are absorbed there. Some others are tracked to the WLS fibers, where they are absorbed and re-emitted at longer wavelengths, allowing them to be tracked toward the SiPM. The number of optical photons detected by each SiPM is recorded event-by-event in ROOT TTree format and analyzed using a C++ code. The simulated data represent the distribution of the number of photons detected by the SiPMs connected to both the upper (x-axis) and lower (y-axis) WLS fibers. In this work, the interaction positions of muons (x, y) are reconstructed using an algorithm developed in-house. The distribution of detected photons is analyzed using the peak search function of the CERN ROOT [30] package.

For each simulated event, the distributions of detected photons in the x and y WLS fibers are analyzed using a peak search function from the ROOT package. The resulting distribution is approximated by a Gaussian function, which is considered as the point of muon impact on the scintillator. The positions of x and y are determined by analyzing the distribution of light photons between the WLS fibers x and y using ROOT tools approximated by a Gaussian function. The uniformity of the 1×1 m^2 plastic scintillator plate response to cosmic ray muons is studied by modeling a 3 GeV muon beam hitting the detector surface in different locations within a 5 cm grid. As shown in Figure 3a, the reconstructed XY coordinates for muon hits are uniformly distributed across the detector surface and reconstructed hit positions correspond to actual positions of the muon beam. The number of detected photons is shown in Figure 3b. As shown in Figure 4a,b, position resolution is slightly better closer to the edge of the scintillator plate.

The mean value of the Gaussian function corresponds to the x- and y-coordinates of the 3 GeV muon beam's interaction position. The spatial resolution, defined as the full width at half maximum (FWHM) of the linear profile, reaches approximately 0.7–0.8 mm (FWHM) at the detector center (Figure 5), and closer to the detector, the edge position resolution is 0.6–0.7 mm (FWHM) (Figure 6).

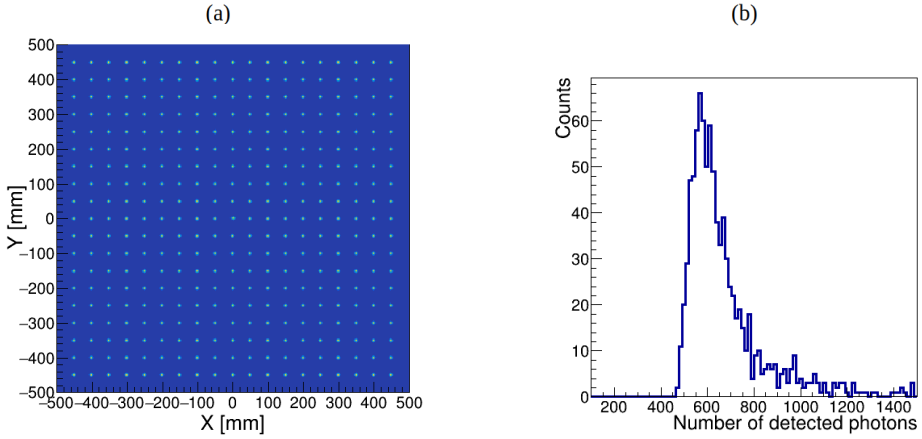

Figure 3. Illustration of uniformity of XY-plane positioning estimation (**a**). Histogram of distribution of detected photons (**b**).

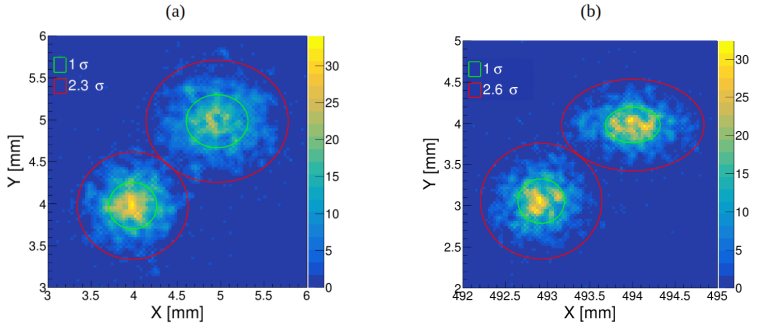

Figure 4. Comparison of position resolution in a central position (muon hit coordinates are $x_1 = 4$ mm, $y_1 = 4$ mm and $x_2 = 5$, $y_2 = 5$ mm) (**a**) and near the detector edge (muon hit coordinates are $x_1 = 493$ mm, $y_1 = 3$ mm and $x_2 = 494$, $y_2 = 4$ mm) (**b**).

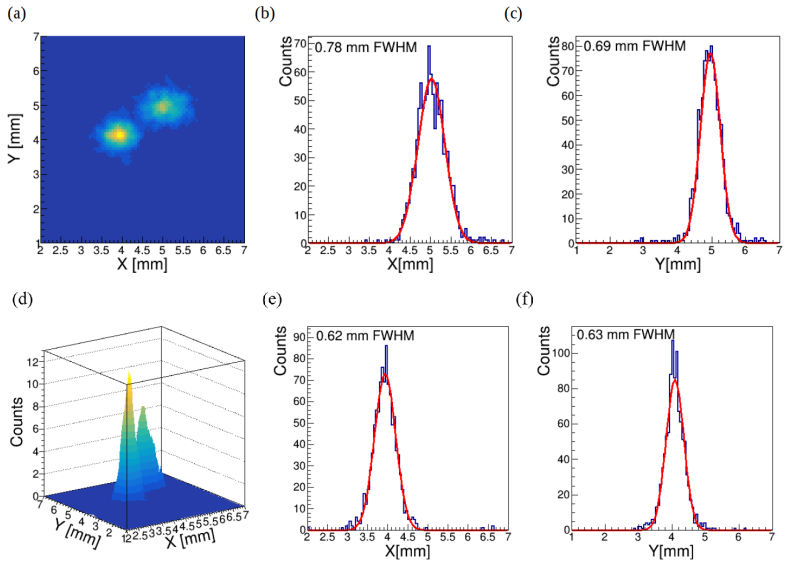

Figure 5. Reconstructed muon interaction position for the central detector area in 2D (**a**) and 3D (**d**) and profiles along the x-axis and y-axis for two beam positions: $x_1 = 4$ mm (**b**), $y_1 = 4$ mm (**c**) and $x_2 = 5$ (**e**), $y_2 = 5$ mm (**f**). The red line shows a Gaussian fit performed on each profile.

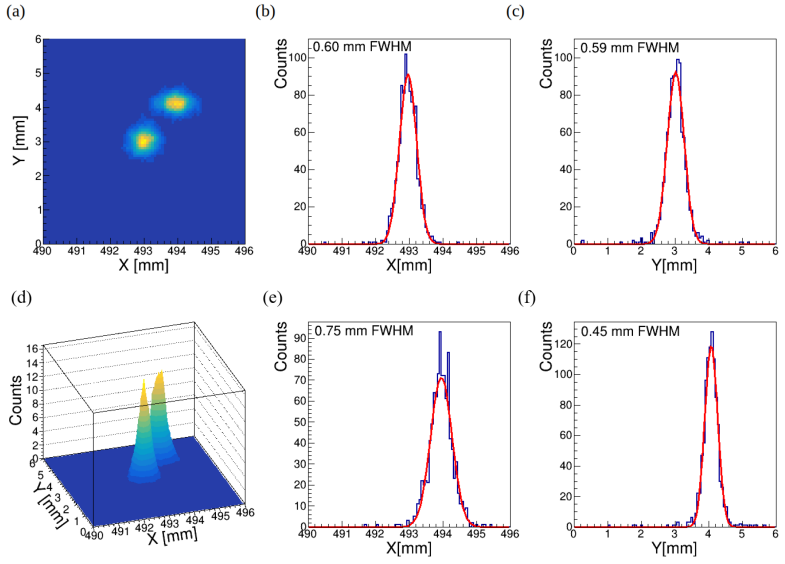

Figure 6. Reconstructed muon interaction position for the central detector area in 2D (**a**) and 3D (**d**) and profiles along the x-axis and y-axis for two beam positions: $x_1 = 493$ mm (**b**), $y_1 = 3$ mm (**c**) and $x_2 = 494$ (**e**), $y_2 = 4$ mm (**f**). The red line shows a Gaussian fit performed on each profile.

4. Cargo Discrimination Capability Study

One of the key tasks of customs and border security is to verify shipping container declarations to prevent illegal trafficking. This can be achieved by comparing the measured data to a customs database or simulated data for scenarios corresponding to the declared contents.

We designed the MTS (see Figure 7) consisting of a matrix of horizontal position-sensitive detectors 1 m × 1 m consisting of a plastic scintillator with a WLSF readout. The interior dimensions of a shipping container are 5.898 m long × 2.352 m wide × 2.393 m high, the usable capacity is 32.6 m^3, and the maximum load is 25 tons. The unloaded weight of a 20-foot container is 2300 kg. In simulations, we consider the container as fully loaded with cargo with a size of 590 cm × 220 cm × 220 cm.

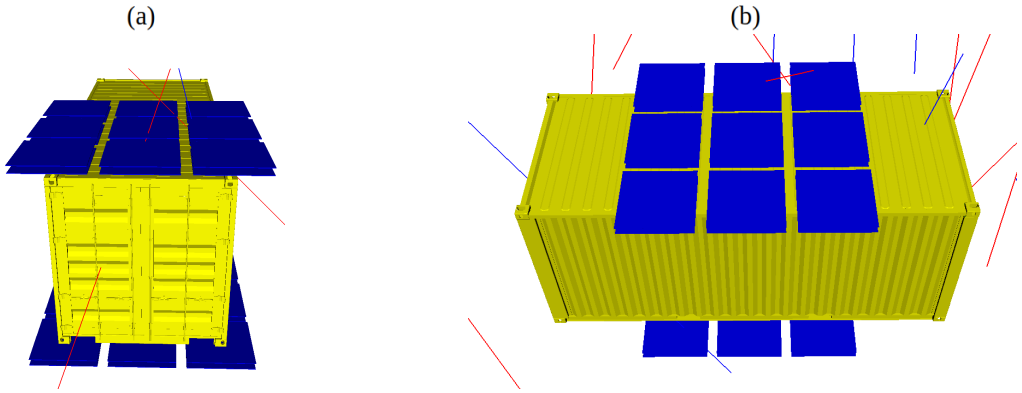

Figure 7. A GEANT4 model of the muon tomography station is illustrated, showing the front view (**a**) and the side view (**b**). The station consists of 9 muon trackers positioned above and 9 positioned below, each constructed from plastic scintillators measuring 1 m × 1 m × 1 cm with the WLS fiber readout. A space is allocated between the plastic scintillator detectors to accommodate the front-end electronics. The muon trajectories are shown as red (μ^-) and blue (μ^+) lines.

4.1. Muon Scattering Tomography

The passage of muons through matter is determined by their interactions with electrons and nuclei. Muon-electron Coulomb interactions result in continuous energy loss, ultimately causing muons to stop and limiting their depth of penetration into a material. Muon–nucleus scattering interactions, induced by the Coulomb fields of nuclei, lead to the angular diffusion of muons. This angular deflection can be analyzed using muon scattering tomography to determine the density and composition of materials. To improve cargo identification and enhance the detection of contraband, we implemented a combined analysis of muon scattering and absorption data. By integrating these two complementary techniques, the combined approach achieves higher material discrimination accuracy compared to using scattering data alone. This improvement is essential for detecting contraband concealed within legitimate cargo and ensuring high throughput in border security applications.

The angular distribution of scattered muons of momentum p is approximately Gaussian, with the zero mean and standard deviation given by

$$\sigma_\theta = \frac{13.6\ \text{MeV}}{\beta c p}\sqrt{\frac{L}{X_0}}\left[1 + 0.038\ln\left(\frac{L}{X_0}\right)\right] \quad (1)$$

where β is the ratio between the velocity of muon v and the velocity of light c, p is the momentum of the muon, X_0 is the radiation length of the material, and L is the length of the material traversed. X_0 is a material property and can be expressed as [31]:

$$X_0 = \frac{716.4\ \mathrm{g/cm^2}}{\rho} \frac{A}{Z(Z+1)\ln(\frac{287}{\sqrt{Z}})} \tag{2}$$

where ρ is the density of the material, A is the atomic mass, and Z is the atomic number. We define the scattering density (λ), derived from the Rossi formula, as [32]

$$\lambda(X_0) = \left(\frac{13.6\ \mathrm{MeV}}{p_0}\right)^2 \frac{1}{X_0} \tag{3}$$

where p_0 is a nominal muon momentum and λ is expressed in milliradians^2/cm. The approximation $\beta c \cong 1$ for muons is used in this equation. The scattering density of a material quantifies the extent to which muons scatter as they traverse a unit depth of the material. This parameter is directly influenced by the material's density and atomic composition, as well as the energy of the muons. In muon tomography, scattering angles are measured and accumulated at different locations within the scanned object, producing a three-dimensional map of scattering densities. The resulting tomographic image provides detailed insights into the internal structure, allowing for the identification of hidden materials, density variations, and anomalies within the scanned volume.

4.2. Muon Absorption Method

The muon absorption tomography technique leverages the fact that muons lose energy as they pass through materials, with the degree of energy loss and the likelihood of muon absorption depending on the material's density and atomic composition. Muon absorption tomography involves counting the muon tracks that generate hits in the upper detectors of a muon tomography station but do not register hits on the lower detectors. This absence of detection in the lower detectors is indicative of muon absorption or scattering events that occur within the imaging volume. By analyzing these events, we can infer the properties of the materials within the volume, as the degree of muon absorption is related to the density and composition of the materials they traverse [22]. The muon absorption tomography technique uses an algorithm that identifies the path of muons based on hit detections. For each muon, the algorithm determines which voxels (3D pixels) the muon trajectory intersects. Each voxel corresponds to a small volume of space within the cargo, and the muon absorption data from these intersections are used to reconstruct a 3D map of the cargo's density and composition. The algorithm keeps track of the number of times each voxel is intersected by muon rays. This traversal counting helps in quantifying the cumulative effect of the material on the muons. By tracking which voxels are hit by muons and which muons do not reach the lower detectors, one can infer properties about the material density and internal structure. For each voxel j, the algorithm calculates the path length d_{ij} that a specific muon i travels through it. This information is critical for evaluating the energy loss experienced by the muons. The stopping power S_j of each voxel signifies the energy lost per unit distance as muons traverse that voxel. It is dependent on the material's physical properties. The total absorption $N_{abs,i}$ along a muon track i can then be given by calculating the sum of the stopping powers of all intersected voxels:

$$N_{abs,i} = \sum_j S_j \cdot d_{ij}. \tag{4}$$

The total absorption of muons provides a measure of how much energy is lost as the muons pass through the cargo. This energy loss can offer valuable insights into the material properties and density variations within the cargo. Voxels with higher absorption rates are typically associated with denser materials. As a result, the reconstructed 3D map can be scaled to represent material density, directly correlating with the observed absorption rates.

4.3. Simulation in a Real Scenario

Contraband materials can be hidden among legal materials, while smuggled material can be declared as legal goods. Such a smuggling scenario is often realized in the case of contraband cigarettes. We simulated this scenario by placing boxes with rolls of towel paper or cigarettes on the floor of a shipping container, thus filling almost all of its free volume. We simulated datasets for a container fully loaded with 5 million cigarettes and a container fully loaded with paper towel rolls.

The Cosmic-Ray Shower Library (CRY) [33] interfaced with GEANT4 was used to generate 200,000 muons for the latitude 50° at sea level, producing one dataset, which corresponded to 20 s of scanning time. The origin points of generated muons were sampled from a horizontal plane surface of 10 m × 10 m. GEANT4 simulates the interaction of muons with the detector, a 20-foot shipping container, and the payload. Simulated data samples were generated by producing 5000 datasets for both paper towel rolls and cigarettes.

The simulated data on hit positions in each detector layer were used to generate two tracks. Cosmic ray muon scattering tomography was achieved by tracking the trajectories of both incoming and outgoing muons using a set of position-sensitive detectors. We calculated the scattering angle between the trajectories of incoming ($\vec{v}_1$) and outgoing ($\vec{v}_2$) muons using the following formula [34]:

$$\theta_{scatt} = arccos\left(\frac{\vec{v}_1 \cdot \vec{v}_2}{|v_1||v_2|}\right). \quad (5)$$

The Point-of-Closest-Approach (PoCA) algorithm [35] was used to reconstruct the position of muon interactions with the cargo and the container. The PoCA algorithm calculates the closest point between the incoming and outgoing muon tracks, which is considered the muon interaction position. The angle between these tracks is regarded as the scattering angle. Figure 8a–c illustrate the reconstructed 3D tomographic image of the cargo (a), created using PoCA points, along with the 2D and 1D profiles (b) and (c) used to calculate the cargo dimensions. Due to the different sizes and loading configurations of the cargo, object detection techniques can be applied to localize and identify the dimensions of the cargo in the reconstructed image of the container [17].

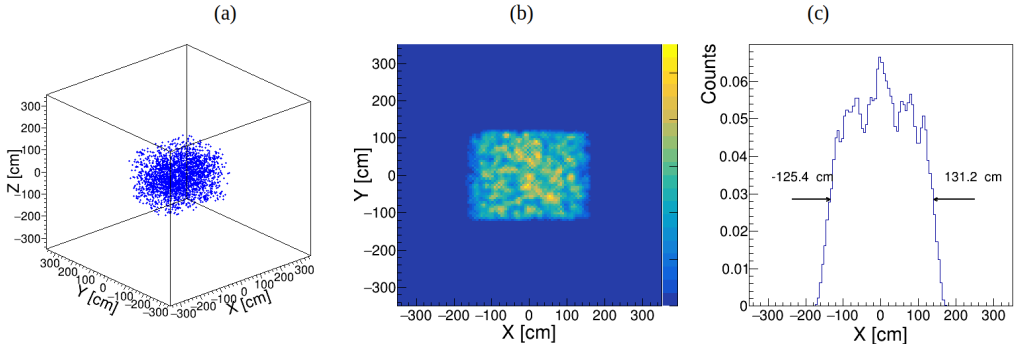

Figure 8. (**a**) Simulated 200k muons (20 s) sampled on a 10 m × 10 m surface using a CRY generator. Three-dimensional image of the PoCA reconstruction of a cigarette smuggling scenario. Two- (**b**) and one-dimensional (**c**) profiles of the PoCA image of tobacco in the compact MTS ($3 \times 3 \times 3$ m^3).

In Figure 9a, the scatter plots of scattering density versus stopped muons distribution are shown for paper towel rolls and tobacco for a detector position resolution of 1 mm (FWHM). On top of the 2D histogram in this figure, the 1D histograms of the scattering distributions for paper towel rolls and tobacco are also shown, while on the right side, we show the histogram of the corresponding scattering-to-stopping ratio distributions. The 1D analysis is limited due to partial overlap between the distributions for paper towel rolls and tobacco, whereas the 2D analysis offers more distinct material discrimination.

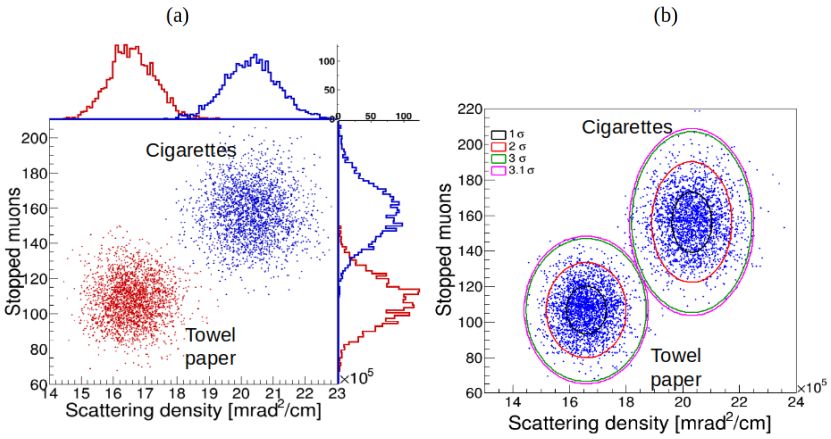

Figure 9. (**a**) Scatter plot showing the distributions of scattering and scattering-to-stopping ratio for paper towel rolls and tobacco. Data points for paper towel rolls are marked in blue, and data points for tobacco are marked in red. (**b**) Scatter plot showing the distributions of scattering density versus stopped muons ratio for paper towel rolls and tobacco in small MTS for 20 s scanning time.

The two-component 2D Gaussian Mixture Model (GMM) algorithm can be used to quantitatively characterize cargo discrimination accuracy. This algorithm segregates the data into distinct groups based on their probability distributions (see Figure 9b). Confidence ellipses are drawn for each distribution, corresponding to 1, 2, and 3 σ confidence levels (CL). The scattering density distribution and stopped muons distribution for rolled paper towels and tobacco are accurately distinguished with a 3 σ CL at a position resolution of 1 mm (FWHM).

5. Conclusions

The detailed geometry of the muon detector, including the layout of the plastic scintillator plates, wavelength-shifting fibers, and SiPMs, is modeled using the GEANT4 toolkit. Simulation results indicate that the proposed detector design, featuring a 1 m $\times$ 1 m scintillator plate readout with 2 mm^2 square-shaped WLS fibers, can achieve a spatial resolution of approximately 0.7–1.0 mm. Taking into account the obtained spatial resolution, the geometric parameters of the muon tomography system were proposed and modeled to optimize performance and accuracy. The CRY package in combination with GEANT4 is used to generate cosmic muons and model their transportation and interaction with the transport container and cargo. The combined analysis of muon absorption and scattering data significantly enhances material discrimination compared to using scattering data alone, thereby reducing measurement time. This improvement is crucial for maintaining high throughput in container inspections. In a smuggling scenario where tobacco is declared as paper towel rolls, it is shown that combined muon scattering and absorption analysis can accurately differentiate between tobacco and paper towel rolls with 3 sigma discrimination for a 1 mm spatial resolution (FWHM) in a short scan time of 20 s using a small-sized (3 m $\times$ 3 m $\times$ 3 m) MTS that covers half of the container. The entire 6 m long shipping container can thus be scanned in 40 s.

Funding: This work was supported by the EU Horizon 2020 Research and Innovation Programme under grant agreement no. 101021812 (“SilentBorder”).

Informed Consent Statement: Not applicable.

Data Availability Statement: The original contributions presented in this study are included in the article. Further inquiries can be directed to the corresponding author.

Conflicts of Interest: The author declares no conflict of interest.

References

1. Bonechi, L.; D'Alessandro, R.; Giammanco, A. Atmospheric muons as an imaging tool. *Rev. Phys.* **2020**, *5*, 100038. [CrossRef]
2. Barnes, S.; Georgadze, A.; Giammanco, A.; Kiisk, M.; Kudryavtsev, V.A.; Lagrange, M.; Pinto, O.L. Cosmic-Ray Tomography for Border Security. *Instruments* **2023**, *7*, 13. [CrossRef]
3. Borozdin, K.N.; Hogan, G.E.; Morris, C.; Priedhorsky, W.C.; Saunders, A.; Schultz, L.J.; Teasdale, M.E. Radiographic imaging with cosmic-ray muons. *Nature* **2003**, *422*, 277–277. [CrossRef] [PubMed]
4. Cuéllar, L.; Borozdin, K.N.; Green, J.A.; Hengartner, N.W.; Morris, C.; Schultz, L.J. Soft cosmic ray tomography for detection of explosives. In Proceedings of the 2009 IEEE Nuclear Science Symposium Conference Record (NSS/MIC), Orlando, FL, USA, 24 October–1 November 2009; pp. 968–970. [CrossRef]
5. Zheng, Y.; Zhi, Z.; Ming, Z.; Wang, X.; Zhao, Z. Discrimination of drugs and explosives in cargo inspections by applying machine learning in muon tomography. *High Power Laser Part. Beams* **2018**, *30*, 086002. [CrossRef]
6. Chen, J.; Li, H.; Li, Y.; Liu, P. Towards a muon scattering tomography system for both low-Z and high-Z materials. *J. Instrum.* **2023**, *18*, P08008. [CrossRef]
7. Schultz, L.J. *Cosmic Ray Muon Radiography*; Portland State University: Portland, OR, USA, 2003.
8. Åström, E.; Bonomi, G.; Calliari, I.; Calvini, P.; Checchia, P.; Donzella, A.; Faraci, E.; Forsberg, F.; Gonella, F.; Hu, X.; et al. Precision measurements of linear scattering density using muon tomography. *J. Instrum.* **2016**, *11*, P07010. [CrossRef]
9. Checchia, P. Review of possible applications of cosmic muon tomography. *J. Instrum.* **2016**, *11*, C12072. [CrossRef]
10. Antonuccio, V.; Bandieramonte, M.; Becciani, U.; Bonanno, D.; Bonanno, G.; Bongiovanni, D.; Fallica, P.; Garozzo, S.; Grillo, A.; La Rocca, P.; et al. The Muon Portal Project: Design and construction of a scanning portal based on muon tomography. *Nucl. Instrum. Methods Phys. Res. Sect. A Accel. Spectrom. Detect. Assoc. Equip.* **2017**, *845*, 322–325. [CrossRef]
11. Pugliatti, C.; Antonuccio, V.; Bandieramonte, M.; Becciani, U.; Belluomo, F.; Belluso, M.; Billotta, S.; Blancato, A.A.; Bonanno, D.L.; Bonanno, G.; et al. Design of a muonic tomographic detector to scan travelling containers. *J. Instrum.* **2014**, *9*, C05029. [CrossRef]
12. Morris, C.; Bacon, J.; Borozdin, K.; Miyadera, H.; Perry, J.; Rose, E.; Watson, S.; White, T.; Aberle, D.; Green, J.A.; et al. A new method for imaging nuclear threats using cosmic ray muons. *AIP Adv.* **2013**, *3*, 082128. [CrossRef]
13. Preziosi, E.; Arcieri, F.; Caltabiano, A.; Camarri, P.; Casagrande, S.; Cavicchioni, D.; Danza, F.A.; Fabrizi, E.; Fabrizi, M.; Festa, G.; et al. TECNOMUSE: A novel, RPC-based, muon tomography scanner for the control of container terminals. *J. Phys. Conf. Ser.* **2020**, *1548*, 012021. [CrossRef]
14. Georgadze, A.S.; Kudryavtsev, V.A. Geant4 simulation study of low-Z material detection using muon tomography. *J. Instrum.* **2023**, *18*, C12014. [CrossRef]
15. Georgadze, A.; Giammanco, A.; Kudryavtsev, V.; Lagrange, M.; Turkoglu, C. A Simulation of a Cosmic Ray Tomography Scanner for Trucks and Shipping Containers. *J. Adv. Instrum. Sci.* **2024**, *2024*, JAIS-482. [CrossRef]
16. Georgadze, A.S. Simulation study into the detection of low- and high-Z materials in cargo containers using cosmic ray muons. *Acta Phys. Pol. B Proc. Suppl.* **2024**, *17*, 1-A2.1–1-A2.8. [CrossRef]
17. Georgadze, A.S. Automated object detection for muon tomography data analysis. *J. Instrum.* **2024**, *19*, C07004. [CrossRef]
18. Europian Commission. *Cosmic Ray Tomograph for Identification of Hazardous and Illegal Goods Hidden in Trucks and Sea Containers*; European Commission: Brussels, Belgium, 2021. [CrossRef]
19. Morris, C.; Borozdin, K.; Bacon, J.; Chen, E.; Lukić, Z.; Milner, E.; Miyadera, H.; Perry, J.; Schwellenbach, D.; Aberle, D.; et al. Obtaining material identification with cosmic ray radiography. *AIP Adv.* **2012**, *2*, 042128. [CrossRef]
20. Blanpied, G.; Kumar, S.; Dorroh, D.; Morgan, C.; Blanpied, I.; Sossong, M.; McKenney, S.; Nelson, B. Material discrimination using scattering and stopping of cosmic ray muons and electrons: Differentiating heavier from lighter metals as well as low-atomic weight materials. *Nucl. Instrum. Methods Phys. Res. Sect. A Accel. Spectrom.Detect. Assoc. Equip.* **2015**, *784*, 352–358. [CrossRef]
21. Vanini, S.; Calvini, P.; Checchia, P.; Rigoni Garola, A.; Klinger, J.; Zumerle, G.; Bonomi, G.; Donzella, A.; Zenoni, A. Muography of different structures using muon scattering and absorption algorithms. *Philos. Trans. R. Soc. A* **2019**, *377*, 20180051. [CrossRef]
22. Georgadze, A.S. Rapid cargo verification with cosmic ray muon scattering and absorption tomography. *J. Instrum.* **2024**, *19*, P10033. [CrossRef]
23. Agostinelli, S.; Allison, J.; Amako, K.; Apostolakis, J.; Araujo, H.; Arce, P.; Asai, M.; Axen, D.; Banerjee, S.; Barrand, G.; et al. GEANT4—A simulation toolkit. *Nucl. Instrum. Methods Phys. Res. Sect. A Accel. Spectrom. Detect. Assoc. Equip.* **2003**, *506*, 506–514. [CrossRef]
24. Geant4 Collaboration. 2025. Available online: https://geant4-userdoc.web.cern.ch/UsersGuides/ForApplicationDeveloper/html/index.html (accessed on 1 January 2025).
25. Gumplinger, P. Optical photon processes in Geant4. In Proceedings of the Users' Workshop at CERN, Stanford, CA, USA, 18–22 February 2002.
26. Vilardi, I.; Braem, A.; Chesi, E.; Ciocia, F.; Colonna, N.; Corsi, F.; Cusanno, F.; De Leo, R.; Dragone, A.; Garibaldi, F.; et al. Optimization of the effective light attenuation length of YAP: Ce and LYSO: Ce crystals for a novel geometrical PET concept. *Nucl. Instrum. Methods Phys. Res. Sect. A Accel. Spectrom. Detect. Assoc. Equip.* **2006**, *564*, 506–514. [CrossRef]

27. Solutions, L. Luxium Solutions. 2024. Available online: https://luxiumsolutions.com/radiation-detection-scintillators/fibers (accessed on 26 December 2024).
28. Georgadze, A.; Shivani, S.; Tayefi, K.A.; Moskal, P. Optimization of the WLS design for positron emission mammography and Total-Body J-PET systems. *Bio-Algorithms Med-Syst.* **2023**, *19*, 114–123. [CrossRef]
29. Solutions, L. Premium Plastic Scintillators, BC-408 Datasheet. 2014. Available online: https://luxiumsolutions.com/radiation-detection-scintillators/plastic-scintillators (accessed on 26 December 2024).
30. Brun, R.; Rademakers, F. ROOT—An object oriented data analysis framework. *Nucl. Instrum. Methods Phys. Res. Sect. A Accel. Spectrom. Detect. Assoc. Equip.* **1997**, *389*, 81–86. [CrossRef]
31. Lynch, G.R.; Dahl, O.I. Approximations to multiple Coulomb scattering. *Nucl. Instrum. Methods Phys. Res. Sect. B Beam Interact. Mater. Atoms* **1991**, *58*, 6–10. [CrossRef]
32. Highland, V.L. Some practical remarks on multiple scattering. *Nucl. Instrum. Methods* **1975**, *129*, 497–499. [CrossRef]
33. Hagmann, C.; Lange, D.; Wright, D. Cosmic-ray shower generator (CRY) for Monte Carlo transport codes. In Proceedings of the 2007 IEEE Nuclear Science Symposium Conference Record, Honolulu, HI, USA, 26 October–3 November 2007; Volume 2, pp. 1143–1146. [CrossRef]
34. Carlisle, T.; Cobb, J.; Neuffer, D. Multiple scattering measurements in the MICE experiment. In Proceedings of the IPAC2012, New Orleans, LA, USA, 20–25 May 2012; Volume 1205201, pp. 1419–1421.
35. Riggi, S.; Antonuccio-Delogu, V.; Bandieramonte, M.; Becciani, U.; Costa, A.; La Rocca, P.; Massimino, P.; Petta, C.; Pistagna, C.; Riggi, F.; et al. Muon tomography imaging algorithms for nuclear threat detection inside large volume containers with the Muon Portal detector. *Nucl. Instrum. Methods Phys. Res. Sect. A Accel. Spectrom. Detect. Assoc. Equip.* **2013**, *728*, 59–68. [CrossRef]